Tailoring of a Phenothiazine Core for Electrical Conductivity and Thermal Stability: Hole-Selective Layers in Perovskite Solar Cells

Peng Huang, [a] Manju, [c] Samrana Kazim, [a,b] Luis Lezama,[d] Rajneesh Misra,[c*] and Shahzada Ahmad [a,b*]

[a] BCMaterials, Basque Center for Materials, Applications and Nanostructures, Martina Casiano, UPV/EHU Science Park, 48940 Leioa, Spain

Tel: +34 946128811 E-mail: shahzada.ahmad@bcmaterials.net;

[b] IKERBASQUE, Basque Foundation for Science, Bilbao, 48013, Spain

[c] Department of Chemistry, Indian Institute of Technology, Indore, India

[d] Departamento de Química Inorgánica, Facultad de Ciencia y Tecnología, Universidad del País Vasco, UPV/EHU, Sarriena s/n, 48940 Leioa, Spain

Abstract

Hole-selective layers are an indispensable component for the fabrication of effective perovskite solar cells. We designed and developed two phenothiazine-based hole transport materials: PTADAnCBZ with an electron-donating sulfur atom and PTODAnCBZ with an electron-withdrawing sulfone group in the core. PTODAnCBZ in contrast to PTADAnCBZ possesses a unique molecular orbital distribution and lower dihedral angles, which endowed it with excellent optoelectrical properties, improved charge transportation, and thermal stability. The solar cells fabricated with PTODAnCBZ yielded a higher photovoltaic (PV) performance as compared to PTADAnCBZ and were on par in terms of performance with those fabricated with Spiro-OMeTAD. Notably, the phenothiazine-based PV devices showed improved stability under multi-stress conditions including moisture, moisture and light, and moisture and heat. Phenothiazine-based molecules showed unparalleled thermal stability as compared to the doped Spiro-OMeTAD.

Our findings pinpoint the advantages of cost-effective phenothiazine with dioxide as hole-selective layers and suggest its application in a variety of optoelectrical devices such as PVs and organic LED.

1. Introduction

New sources for energy generation are essential for our society, and emerging photovoltaics (PVs) based on perovskites have been shown to have unparalleled performance by the research community during the last decade. The astonishing performance of perovskite solar cells (PSCs) stems from the high defect tolerance and excellent optoelectrical properties of the perovskites.[1,2] In a typical PSC, the perovskite as a light harvester is sandwiched between electron- and hole-transporting materials (ETMs, HTMs). The role of charge selective layers is to extract and transport photogenerated charge carrier and suppress charge carriers recombination in perovskite and at the perovskite/ETM and perovskite/HTM interface.[3,4] Although HTM-free-based PSCs can also be fabricated and gave competitive power conversion efficiency (PCE),[5] however its suitability in terms of performance as compared to the device with charge selective layers is improbable. HTMs employment have been identified as a significant contributor to facilitate hole extraction, inhibiting ion migrations, reduce abnormal hysteresis behaviour as well as hinder the degradation of perovskite.[4,6–8]

Presently, *2,2′,7,7′*-tetrakis-(*N,N*-di-p-methoxyphenylamine)-*9,9′*-spirobifluorene (Spiro-OMeTAD) is used as benchmark HTM and enjoy the privilege being the most efficient state of the art for PSCs.[6,89] However, the apparent shortcomings, such as complex synthetic procedure, high cost, and low transporting ability, are considered as constrain in scale up of the PSCs. Small molecules based on organic semiconductors are potentially attractive alternatives for Spiro-

OMeTAD, and its merits include low batch-to-batch variations, tuneable molecular structure, cost efficient, and simplified purification process.[10–14]

Among them, the phenothiazine (PTZ)-based HTMs have emerged in the arena of HSLs as an alternative to Spiro-OMeTAD.[1516] Phenothiazine with nitrogen and sulfur heteroatoms is a prominent electron-rich heterocyclic compound and yields a stable radical cation, reversible electrochemical oxidation, and low ionization potential. Furthermore, the butterfly type molecular confirmation of the phenothiazine ring will block molecular aggregation.[17] Besides, the diversity of reactive sites including *3-*, *7-* and *S-*, *N-*position of phenothiazine make the extra effect to customize a library of HTMs. Such characteristics allow the use of PTZ-based HTMs in PSCs fabrication. Rationally designed Spiro[fluorene-9,9′-xanthene]-based HTM employing PTZ as arms,[18] and PTZ1/PTZ2 HTMs, where PTZ with *N-*position substituting anisole (PTA) as core have been reported.[16] Furthermore, in a recent report, phenothiazine 5,5-66 dioxide derivatives with N-position substituting anisole (PTO) and 4,4-dimethoxy-triphenylamine was revealed as versatile to PTO oxidized from a PTA building block.[19] Arguably, it would be remarkable to investigate PTO-based HSLs, particularly considering the passivation function by sulfone. Importantly, the conversion of an electron-donating sulfur atom to an electron-withdrawing sulfone group impacts materials properties and its influence on the fabricated devices is hereto not investigated.

Herein, we designed and developed PTADAnCBZ and PTODAnCBZ comprising PTA and PTO with N-position substituting anisole as the core and DAnCBZ as the end arms at the 3-, 7-position of the core as the HSL for PSC fabrication (DAnCBZ stands for bis(N 79 3,N3,N6,N6-tetrakis (4-methoxy-phenyl)-9H-carbazole-3,6-diamine). The π-electrons are delocalized over the π-conjugated group carbazole through long pair electrons at the N atoms in DAnCBZ.[20] Besides,

the benefits of using DAnCBZ as an arm are as follows: (i) cost- 84 competitive, (ii) attractive electro-optical properties, (iii) thermal and morphological stability, and (iv) suitable energy levels.[21–23]To scrutinize the structure−property relationships affected by the electron-donating sulfur atom and electron-withdrawing sulfone groups, the synthetic procedure, thermal stability, electrochemical properties, electrical properties, density functional theory (DFT), film-forming ability, PV properties, and stability under multi-stress performance of PSCs using innovative HTMs were methodically investigated via an array of techniques.

2. Results and discussion

2.1 Synthesis

The synthetic protocols for the **PTADAnCBZ** and **PTODAnCBZ** are represented in Scheme 1, and step-by-step synthetic procedures and characterization data are documented in the experimental section (Supporting Information). The intermediate **DAnCBZ** is a carbazole derivative modified with 4,4'-dimethoxydiphenylamine and was synthesized through bromination of carbazole followed by the Pd-catalyzed C-N coupling reaction. The desired molecule 9,9'-(10-(4-methoxyphenyl)-10H-phenothiazine-3,7-diyl)bis(N^3,N^3,N^6,N^6-tetrakis(4-methoxyphenyl)-9H-carbazole-3,6-diamine) named as **PTADAnCBZ** was synthesized from Pd-catalyzed Buchwald−Hartwig cross-coupling reaction of **DAnCBZ** with 3,7-dibromo-10-(4-methoxyphenyl)-10H-phenothiazine (**PTA-Br)** in 49% yield. Similarly, the **PTODAnCBZ** was synthesized by the Pd-catalysed Buchwald–Hartwig cross-coupling reaction of **DAnCBZ** with 3,7-dibromo-10-(4-methoxyphenyl)-10H-phenothiazine 5,5-dioxide (**PTO-Br)** in 50% yield. [16,24,25] Both **PTADAnCBZ** and **PTODAnCBZ** molecules are soluble in common organic solvents such as tetrahydrofuran, chloroform, dichloromethane, chlorobenzene, *etc.* and were characterized

by different spectroscopic techniques such as ^{1}H NMR, ^{13}C NMR and mass spectrometry (Figures S1-S6).
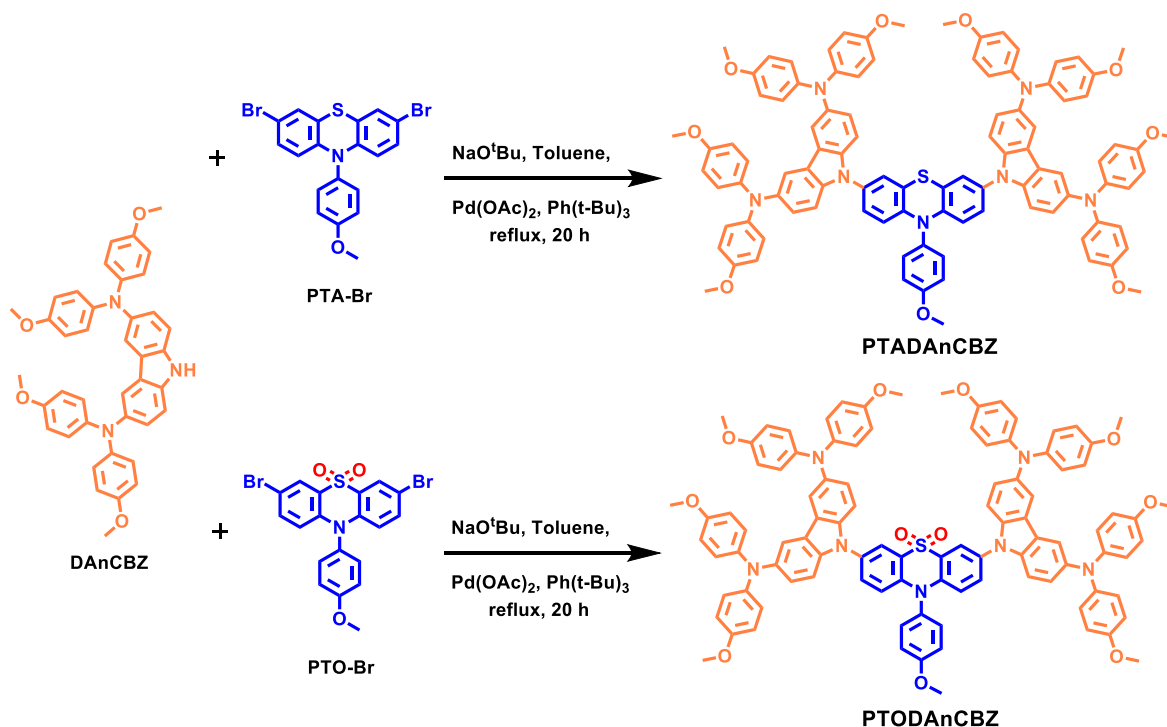
Scheme 1. Synthetic route for the preparation of **PTADAnCBZ** and **PTODAnCBZ**.

2.2 Photophysical and Electrochemical Properties

The normalized electronic absorption spectra of **PTADAnCBZ** and **PTODAnCBZ** in dichloromethane are shown (Figure 1a) and the data are compiled in Table 1. **PTADAnCBZ** and **PTODAnCBZ** show three absorption bands in the UV-visible region, in which the first two absorption bands around 294 nm, 309 nm and 291 nm, 308 nm, corresponds to the π-π* electronic transitions, whereas the absorption bands in the longer wavelength region around 346 nm and 365 nm, attributed to the intramolecular charge transfer (ICT) transitions. A bathochromic shift of 19

nm was deduced for the absorption bands of **PTODAnCBZ** as compared to **PTADAnCBZ**, which is ascribed due to the electron-withdrawing sulfone group in **PTODAnCBZ**. The optical bandgaps (E_g^{opt}) of HTMs are determined by using the equation ($E_g^{opt} = 1240/\lambda_{onset}$), in which λ_{onset} represents the edge of the absorption spectra at long wavelength region. The λ_{onset} of **PTADAnCBZ** and **PTODAnCBZ** are 346 nm and 365 nm, relating to the E_g^{opt} of 2.98 eV and 2.87 eV, respectively.

We probed the electronic features of the highest occupied molecular orbital energy level (E_{HOMO}) using cyclic voltammetry (CV), in dicholormethane using 0.1 M tetrabutylammonium hexafluorophosphate as the supporting electrolyte, platinum wire as counter electrode, and saturated calomel electrode as a reference electrode. The CV curves of **PTADAnCBZ** and **PTODAnCBZ** (Figure 1b) show two highly reversible oxidation potentials, indicating outstanding electrochemical stability, corresponding to the formation of the radical cation of the carbazole moiety and the dication quinonediimine, respectively. The E_{HOMO} of **PTADAnCBZ** and **PTODAnCBZ** are at − 5.58 eV and − 5.62 eV, respectively, calculated from $E_{HOMO} = -5.11 -$ ($E_{ox}^{1/2}$ vs Fc/Fc$^+$), where ($E_{ox}^{1/2}$ vs Fc/Fc$^+$) is the first half-wave oxidation value of the first oxidation waves. The lowest unoccupied molecular orbital (E_{LOMO}) of **PTADAnCBZ** and **PTODAnCBZ** are at − 2.97 eV and − 2.87 eV, respectively, calculated the following equation ($E_{LOMO} = E_{HOMO} - E_g^{opt}$). The values of E_{HOMO} and E_{LOMO} energy levels of **PTADAnCBZ** and **PTODAnCBZ** are summarized in Table 1.[24,26]

In the energy level diagram of the fabricated PSCs (Figure S7), the E_{HUMO} values of **PTADAnCBZ** and **PTODAnCBZ** are located in between valence band maximum of mixed-cation perovskite (−5.9 eV) and gold electrode (−5.1 eV), and **PTODAnCBZ** is slightly higher than that of **PTADAnCBZ**, illustrating favourable hole transportation and estimated to yield higher open-circuit voltage (V_{oc}).[27] Besides, the E_{LUMO} values are much higher than the conduction

band minimum of perovskite, the large barrier between them blocks the possible electron transfer and impedes the charge recombination at the perovskite/HSL interfaces.
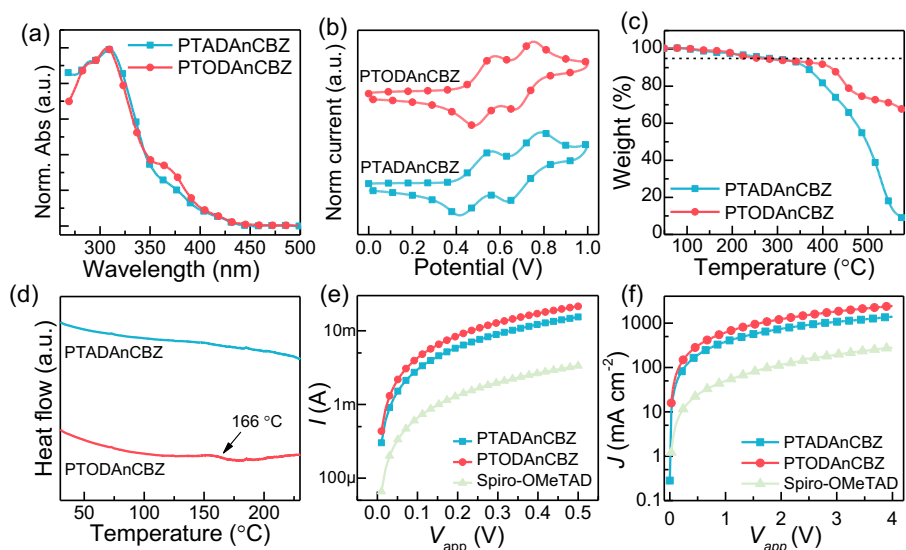

Figure 1. a) UV-vis absorption spectra of **PTADAnCBZ** and **PTODAnCBZ** in dichloromethane, b) CV curves of **PTADAnCBZ** and **PTODAnCBZ**, c) TGA curves of **PTADAnCBZ** and **PTODAnCBZ** at a heating rate of 5 ºC min⁻¹ under a nitrogen atmosphere, d) differential scanning calorimetry curves of **PTADAnCBZ** and **PTODAnCBZ** at a rate of 10 ºC min⁻¹, e) *I-V* curves for conductivity measurement based on devices with a structure: ITO/HTM/Ag and f) *J-V* curves for hole mobility measurement with the hole-only device with a structure: ITO/PEDOT:PSS/HTM/Au.

Table 1. Optoelectrical, thermal, electrochemical and electrical properties of **PTADAnCBZ** and **PTODAnCBZ**.

HTM	$\lambda_{max}/\lambda_{onset}$ (nm)	E_g^{opt}/E_g^b	E_{HOMO} (eV)	E_{LUMO} (eV)	T_d (ºC)	T_g (ºC)	Conductivity[c] (μS cm⁻¹)	Mobility[c] (10^{-4} cm²V⁻¹s⁻¹)
PTADAnCBZ	294,309,346/416	2.98/3.48	-5.58[a]/-4.29[b]	-2.60[a]/-0.81[b]	285	-	3.1	0.92
PTODAnCBZ	291,308,365/432	2.87/3.35	-5.62[a]/-4.25[b]	-2.75[a]/-0.90[b]	265	166	4.5	2.18

$^aE_{HOMO}$, $E_{LUMO,}$ and bandgap estimated from the redox potential in cyclic voltammetry and UV–vis absorption spectra; ^{b}DFT calculations of HTMs: $E_g = E_{HUMO} - E_{LOMO}$. ^{c}HTMs without dopants.

We evaluated the thermal stability of the developed HTMs by thermogravimetric (TGA) and differential scanning calorimetry (DSC) measurements. The TGA curves of **PTADAnCBZ** and **PTODAnCBZ (**Figure 1c) exhibit decomposition temperatures close to 285 °C and 265 °C, respectively (5% weight loss), affirming its thermal stability. The second-heating run DSC curves (Figure 1d) of **PTADAnCBZ** and **PTODAnCBZ** reveal its amorphous nature. No sign of glass transition temperature (T_g), was deduced for PTADAnCBZ, while PTODAnCBZ shows a T_g at 166.5 °C, which is higher than that of conventional Spiro-OMeTAD (~ 127 °C).[28] The creditable thermal stability of **PTADAnCBZ** and **PTODAnCBZ** will ensure the success of the fabricated perovskite-based device operation at extreme conditions (> 85 ºC).

We investigated the influence of dioxide implantation at *S*-position in **PTODAnCBZ** on electrical properties was investigated according to our reported electrical measurement protocol.[12,21,29] The conductivity of pristine HTMs was derived by measuring the linear current-voltage curves of the device (ITO/HTM/Ag). The conductivity of **PTADAnCBZ** and **PTODAnCBZ** were ~ 3.1 and ~ 4.5 μS cm^{-1}, respectively, which is higher than of pristine Spiro-OMeTAD with 1.0 μS cm^{-1}. The hole mobilities of pristine **PTADAnCBZ, PTODAnCBZ, and Spiro-OMeTAD HTMs were** 0.92×10^{-4}, 2.18×10^{-4}, and 1.13×10^{-4} cm^2 V^{-1} s^{-1}, respectively, which was derived by fitting the $J^{1/2}$–V curves obtained from hole-only devices following the Mott-Gurney square law ($J=9\varepsilon\varepsilon_0\mu V_{app}^2/8L^3$). The values of pristine Spiro-OMeTAD are compatible with the literature.[13,30] **PTODAnCBZ** gave higher mobility value than of **PTADAnCBZ** and Spiro-

OMeTAD, owing to the improved intramolecular charge transfer affected by the introduction of dioxide.

To quantify the molecular orbital distribution of **PTADAnCBZ** and **PTODAnCBZ**, the frontier molecular orbitals were calculated at the B3LYP/6-31G(d) level (**Figure 2a)** and summarized in Table 1. The E_{HOMO} levels of **PTADAnCBZ** and **PTODAnCBZ** are located on the **DAnCBZ** groups (arms), while the E_{LOMO} levels were mainly delocated on the phenothiazine (core). The E_{HOMO} values of **PTADAnCBZ** and **PTODAnCBZ** determined from the theoretical studies are – 4.29 eV and – 4.25 eV, respectively, while the E_{LUMO} level of **PTADAnCBZ** and **PTODAnCBZ** is – 0.81 eV and – 0.90 eV, respectively. In the case of **PTADAnCBZ**, the E_{LUMO} is localized over the entire phenothiazine moiety, however, the E_{LUMO} level of **PTODAnCBZ** remains on the sulfone part that could be due to the higher acceptor strength of sulfone as compared to the sulphur atom. We calculated the dihedral angle to unravel the planarity of the molecules. The amine-substituted carbazole units display twisted geometries vis-à-vis the central phenothiazine core (Figure 2b). The **PTODAnCBZ** with 52.55° and 49.27° dihedral angles owns a lower level of planarity as compared to **PTADAnCBZ** with 52.40° and 73.93° (Figure 2b), which reduce the molecular stacking and helps in the formation of uniform film in **PTODAnCBZ**.[21,31]
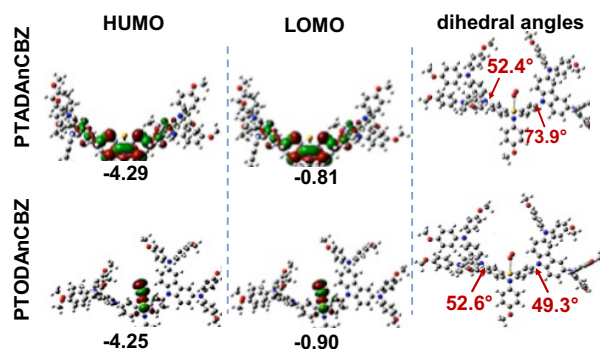
Figure 2. a) Energy level diagram showing the HOMO and LUMO levels of **PTADAnCBZ** and **PTODAnCBZ** as determined at the B3LYP/6-31G(d) level and b) the dihedral angles of **PTADAnCBZ** and **PTODAnCBZ**.

The X-band EPR spectra recorded on solid samples of both compounds show complex signals with low intensity. It was essential to accumulate 30 spectra to obtain the signals recorded (Figure 3**)**. The intensity of the signals decreases rapidly with lowering the temperature due to saturation effects. Solid state Q-band experiments suggest that a partially resolved hyperfine structure is responsible for the shoulders observed over the main lines. To confirm this hypothesis, we recorded the EPR spectra in toluene solutions. In these, three lines are observed with intensity ratios close to 1:1:1, as corresponds to the hyperfine splitting caused by a ^{14}N nucleus (I=1). Arguably, we can be conclude that the unpaired electron is located mainly on the nitrogen atom of the phenothiazine entities. We have not observed, hyperfine interactions with lateral protons, and we speculate that the value of their coupling constants must be less than the line widths of the peaks.
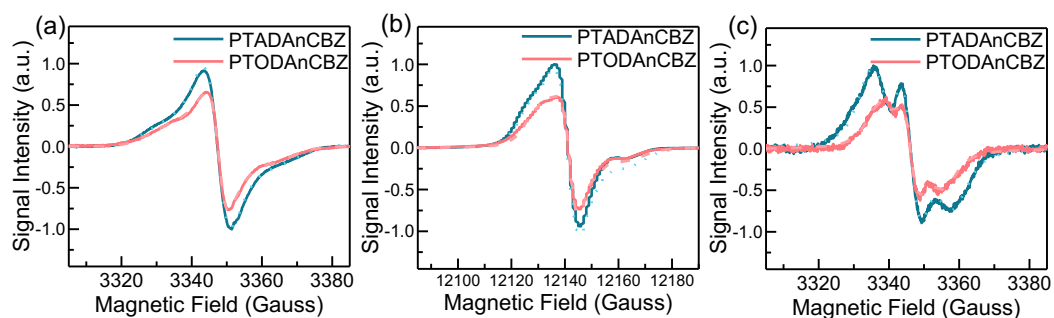

Figure 3. Room-temperature spectra recorded on (a,b) powder samples (a) X-band and (b) Q Band and (c) in toluene solutions. The dotted lines represent the best fits obtained and were calculated with the spectral parameters listed in Table S1.

The spin Hamiltonian parameters were determined by a computer simulation program working at the second order of the perturbation theory (Table 2). Both compounds show practically axial symmetry in the g and A tensors according with a essentially planar cation radical. The principal values of g and A are close to those observed for the phenothiazine cation radical $(PTAZ^+)$[32]. It should be noted that the value of the hyperfine coupling constant a^N is significantly lower for PTODAnCBZ (a^N= 5.7 Gauss) than for compound PTADAnCBZ (7.4 Gauss), is in good agreement with the reduction of the electron density in the phothiazine ring causes by the strongly electronegative SO_2 group.

We probed the film-forming abilities of the **PTADAnCBZ** and **PTODAnCBZ** to ascertain the molecular assembling before introduction into devices. The target HTM samples were prepared by spin-coating the HTM precursor solution containing dopants (Li-TFSI and *t*-BP) on the top of the mixed-cation perovskite with the *b&mp*-TiO$_2$ scaffold for surface morphology measurements with the scanning electron microscope (SEM) and atomic force microscope (AFM) (*b&mp*-TiO$_2$ denotes blocking and meso-porous TiO$_2$ layer) (Figure S8). The microstructure image of the top-surface of perovskite film showed the perovskite grains and PbI_2 crystals, and the perovskite with HTMs presents the continuous and uniform HTMs perfectly cover the bare perovskite. From the topography image, we deduce perovskite display rough surface with high root-mean-square (RMS) value (18.7 nm), while perovskite/**PTADAnCBZ** and perovskite/**PTODAnCBZ** showed a relatively smooth surface with RMS value of 6.3 nm and 6.1 nm, respectively. A trivial difference affected by the dioxide on the core was observed. The uniform coverage and rms decrement indicate the interfacial contact between perovskite/HSL to favour device performance.

2.3 Device performance

11

To elucidate the impacts of **PTODAnCBZ** containing dioxide on the PV performance of PSCs, we fabricated devices with a FTO/*b&mp*-TiO$_2$/perovskite/HTM/Au configuration. The device architect and the corresponding cross-sectional SEM image of the PSC with **PTADAnCBZ** as an HSL is shown (Figure 4a**)** reveal an interconnected and layered configuration with a $\sim$ 440 nm-thick perovskite film and $\sim$ 105 nm **PTADAnCBZ** films.
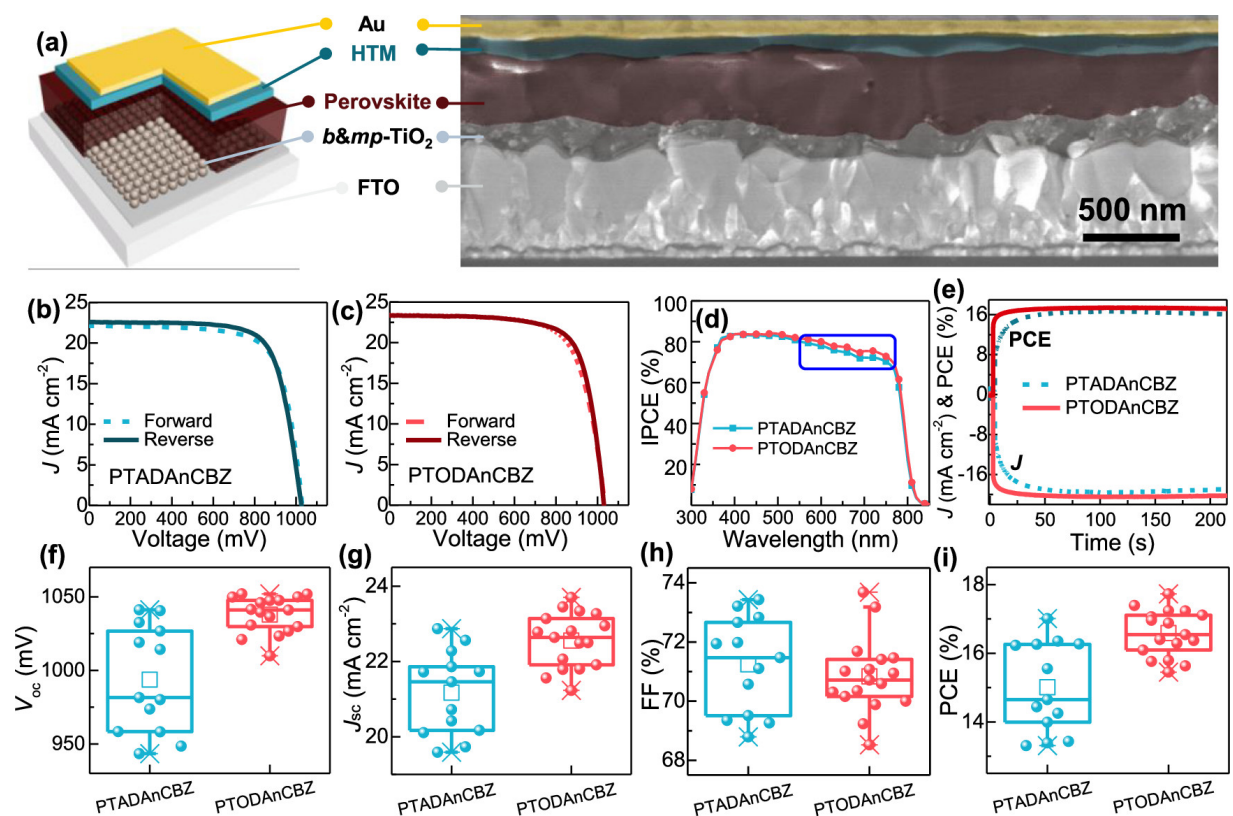

Figure 4. a) Device structure and the corresponding cross-sectional SEM image of the PSCs with **PTADAnCBZ**. *J-V* curves of the PSC with b) **PTADAnCBZ** and c) **PTODAnCBZ** measured by forward and reverse scans under simulated AM 1.5G illumination, d) corresponding EQE curves, e) stabilized power output of PSCs with **PTODAnCBZ** and **PTADAnCBZ**. The statistical *PV* parameters, f) V_{oc}, g) J_{sc}, h) FF, and i) PCE of devices with **PTADAnCBZ** and **PTODAnCBZ**.

The figures of merit for PSCs with doped **PTADAnCBZ** and **PTODAnCBZ** are illustrated (Figure 4b,c), and the detailed PV parameters are summarized in Table 2. The **PTODAnCBZ** based PSC displayed a PCE of 17.73%, with a V_{oc} of 1030.8 mV, a short-circuit current (J_{sc}) of 23.34 mA cm^{-2}, and a fill factor (*FF*) of 73.7%, while the **PTADAnCBZ** based PSC gave a relatively lower PCE of 17.01%, with a V_{oc} of 1026.7 mV, a J_{sc} of 22.56 mA cm^{-2} and an *FF* of 73.4%. The J_{sc} values are in agreement with the external quantum efficiency (EQE) results as (Figure 3d) and integrated current density (Figure S9). The PSC with **PTODAnCBZ** displayed a slightly higher EQE value at the long-wavelength (600 nm – 800 nm) than that of **PTADAnCBZ** marked by blue frame. We ascribed this due to the perovskite with different HTMs, display similar absorption curves (Figure S10), and the improved EQE and J_{sc} stems from faster charge carrier transportation and suppression of recombination occurring at the perovskite/HTMs interface. The PCE of PSCs employing **PTODAnCBZ** is comparable with that of Spiro-OMeTAD (Figure S11 in the Supporting Information) , suggesting its effectiveness as a promising HTM.

Hysteresis analysis was used to evaluate their performance by measuring device under forward scan (FS) and reverse scan (RS), and hysteresis index (*HI*) was estimated according to the equation below: $HI = [J_{RS}(0.8V_{oc}) - J_{FS}(0.8V_{oc})]/J_{RS}(0.8V_{oc})$, where $J_{RS}(0.8V_{oc})$ and $J_{FS}(0.8V_{oc})$ represent the current density of *J-V* curves obtained by RS and FS at 80% of V_{oc}, respectively.[8,33] The *HI* for the PSC with **PTADAnCBZ** and **PTODAnCBZ** is 1.5% and 3.9%, respectively, and we attribute the decreased *HI* for the **PTODAnCBZ**-based PSCs to the improved charge transport ability induced by the use of sulfones in the place sulphide derivative **PTADAnCBZ**. We tracked the PSCs for stabilized power output with different HTMs at maximum power point. PSC based on **PTODAnCBZ** gave the stabilized PCE with ~ 17.7% instantly, whereas **PTODAnCBZ**-based

device exhibited ~ 16.3% over 50 s (Figure 3e). This signals that the PSCs with **PTODAnCBZ** possesses low defect densities, suppressed hysteresis and lower activation energy.

The statistical PV parameters of devices with **PTADAnCBZ** and **PTODAnCBZ** were analysed (Figure 4f −4i). The average V_{oc} values from **PTADAnCBZ** with 1037.9 mV are higher than that of **PTADAnCBZ** (993.7 mV) based PSCs, which we ascribed to the aligned energy level between **PTODAnCBZ** and perovskite. The relatively narrow distribution of V_{oc} and J_{sc} leads to identical PCE performance for **PTODAnCBZ**-based PSCs.

Table 2. The PV parameters of the PSCs with different HTMs.

HTM		V_{oc} (mV)	J_{sc} (mA cm^{-2})	FF (%)	PCE (%)
PTADAnCBZ	FS	1029.1	22.16	72.6	16.56
	RS	1026.7	22.56	73.4	17.01
	average	993.7±35.0	21.17±1.06	71.2±1.6	15.01±1.26
PTODAnCBZ	FS	1036.6	23.40	70.9	17.19
	RS	1030.8	23.34	73.7	17.73
	average	1037.9±12.1	22.56±0.70	70.8±1.2	16.58±0.66

The static photoluminescence (PL) measurements was performed to analyse the charge carrier separation and transport process, occurring in HTM with different core on the corresponding PV performance. The samples for PL measurement were prepared in a similar fashion as for the device, i.e. HTM was deposited atop of quartz/perovskite. The bare perovskite yielded a strong PL emission with the peak at 803 nm, while the perovskite with HTMs showed reduced PL intensity and blue-shifted peak (**Figure 5a**), indicating that the HTMs facilitate hole extraction and transport toward the metal electrode and a decrease in the surface trap states of perovskite.[35]
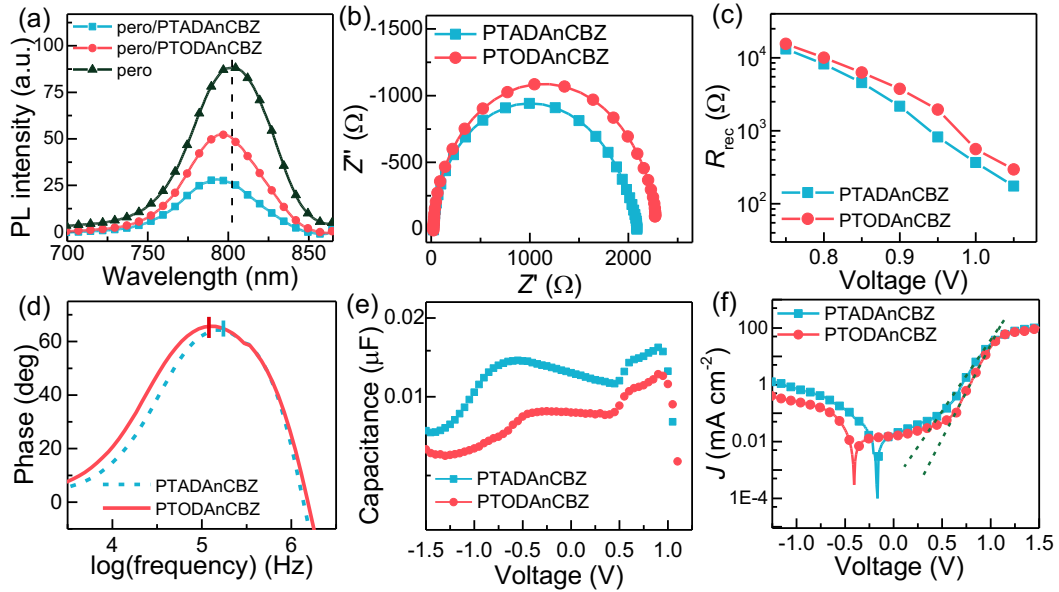
Figure 5. a) Static photoluminescence for bare perovskite, perovskite with **PTADAnCBZ** and **PTODAnCBZ**, b) typical Nyquist plots of the device with **PTADAnCBZ** and **PTODAnCBZ** HTMs with V_{app} = 0.95 V, c) recombination resistance extracted from Nyquist plots of the PSC under different V_{app} and dark conditions, d) bode plot for **PTADAnCBZ** and **PTODAnCBZ** based PSC measured at 1.0 V bias voltage (near to V_{oc}) under dark condition, e) *C-V* characteristics with **PTADAnCBZ** and **PTODAnCBZ** and f) *J-V* curves for the PSC with **PTADAnCBZ** and **PTODAnCBZ** measured under dark conditions.

To elucidate the charge transport kinetics such as recombination at surface/grain boundaries, charge carrier extraction/transportation in PSCs with different HTMs, we performed electrical impedance spectroscopy (EIS). The typical Nyquist plots with the applied bias voltage (V_{app} = 0.9 V) are shown (Figure 5b), and fitted by an equivalent circuit modelling ($R–R_{rec}\|C$, (Figure S12 in the supporting information), where R, $R_{rec}\|C$ represents the series resistance of the external circuit, recombination resistance, and capacitance, respectively. The R_{rec} values of the device with HTMs

under different V_{app} varied from 0.75 V to 1.05 V, with a step of 0.05 V was extracted and plotted (Figure 5c). With the increase of V_{app}, the R_{rec} values decreases sharply, owing to the continuously improving carrier concentration. The R_{rec} value for the **PTODAnCBZ**-is higher than of **PTADAnCBZ**- based PSC, implying that the **PTODAnCBZ** significantly reduces charge recombination at the perovskite/HTM interface. Further, we estimated the charge lifetime (τ) of the device with different HTM by analysing the Bode plot at the V_{app} (near V_{oc}) following the equation: $\tau = 1/(2\pi f_p)$, where f_p is the frequency of the peak (marked in the Figure 5d), corresponding to the electrochemical reaction of the charge transfer process at perovskite/HTM interface.[35] The τ values for **PTADAnCBZ**- and **PTODAnCBZ**-based PSCs are 0.96 μs and 1.29 μs, respectively. The longer τ value of **PTODAnCBZ**-based PSCs can be ascribed to the improved electron density and rapid charge carrier at the perovskite/**PTODAnCBZ** interface, which agrees with the high hole-mobility of the same.

We measured the capacitance-voltage (*C-V*) characteristics at V_{app} varying from -1.5 V to 1.25 V. Accordingly, the capacitance is induced by electron trap states at the interface and delocalizing charge carriers. The capacitance of **PTODAnCBZ** was lower than that of **PTADAnCBZ** (Figure 5e) and the reduced capacitance implies that the trap states decreases the photogenerated carrier extraction. The *J-V* curves measurement under dark conditions suggests the intrinsic properties of the PV. The dark *J-V* of PSC with **PTADAnCBZ** and **PTODAnCBZ** was measured and semilogarithmic plots is shown (Figure 5f). The leakage current (under negative bias) in the **PTODAnCBZ** is lower than that of the **PTADAnCBZ**, leading to higher J_{sc}. The linear parts of the dark *J-V* were fitted with the Shockley diode equation: $J_D = J_0[\exp(qV/nK_BT)-1]$, where J_0 is the reverse saturation current density, J_D is the dark current density, V is the applied bias, q is the electron charge, K_B is the Boltzmann constant, T is the temperature, n is the ideal

factor of the real diode.[37,38] For PSCs with different **PTADAnCBZ** and **PTODAnCBZ**, n and J_0 are listed in Table S2. The values of [n, J_0] were [3.35, 3.26×10^{-4} mA cm^{-2}] and [2.63, 9.78×10^{-6} mA cm^{-2}] for the PSCs based on **PTADAnCBZ** and **PTODAnCBZ**, respectively. The smaller values of the n and J_0 for **PTODAnCBZ**-based PSCs signals a suppressed interfacial recombination, which, in turn, increases the charge transportability to deliver an improved performance.[38]

2.4 Stability Performance

Device stability and performance, is a crucial aspect in evaluating PV reliability. Arguably, the PSCs should perform under multi-stress conditions such as continuous light, moisture, and heat. We investigated PSCs with **PTADAnCBZ** and **PTODAnCBZ** under multi-stress conditions and compared it with Spiro-OMeTAD.

Firstly, the unencapsulated PSCs were measured under ambient condition with 30 – 70% relative humidity (RH) and room temperature (Figure 6a). The PCEs for **PTADAnCBZ-** and **PTODAnCBZ**-based PSC maintained 74.8% and 76.3% of their initial value, respectively, after aging for 1,100 h, while for the PSCs with Spiro-OMeTAD, it lost 60% of its initial PCE after 700 h. The *FF* of devices with **PTADAnCBZ** and **PTODAnCBZ** HTMs retained 77.8% and 89.8% of initial values after 1,100 h, while the control device reduced to 74.9% after 700 h (Figure S13a). The series resistance (R_s) of PSCs slightly increases to 1.3 times of its initial values, while for PSCs with SpiroOMeTAD it triplicates (Figure S13b). The FF is impacted by the R_s, and the increasing trend can be explained by the decreasing FF. More importantly, we tracked the absorption spectra of the perovskite with different HTMs and the normalized absorption intensity at 600 nm (Figure S13c). The perovskite with phenothiazine based HTMs showed higher absorbance than that of control films after aging. Our results suggests that **PTADAnCBZ** and

PTODAnCBZ hold the judicious properties and perovskite/HTM interface during aging, while the Spiro-OMeTAD owned poor intrinsic stability, causing deterioration of the interface, and accelerate the decomposition of perovskite.
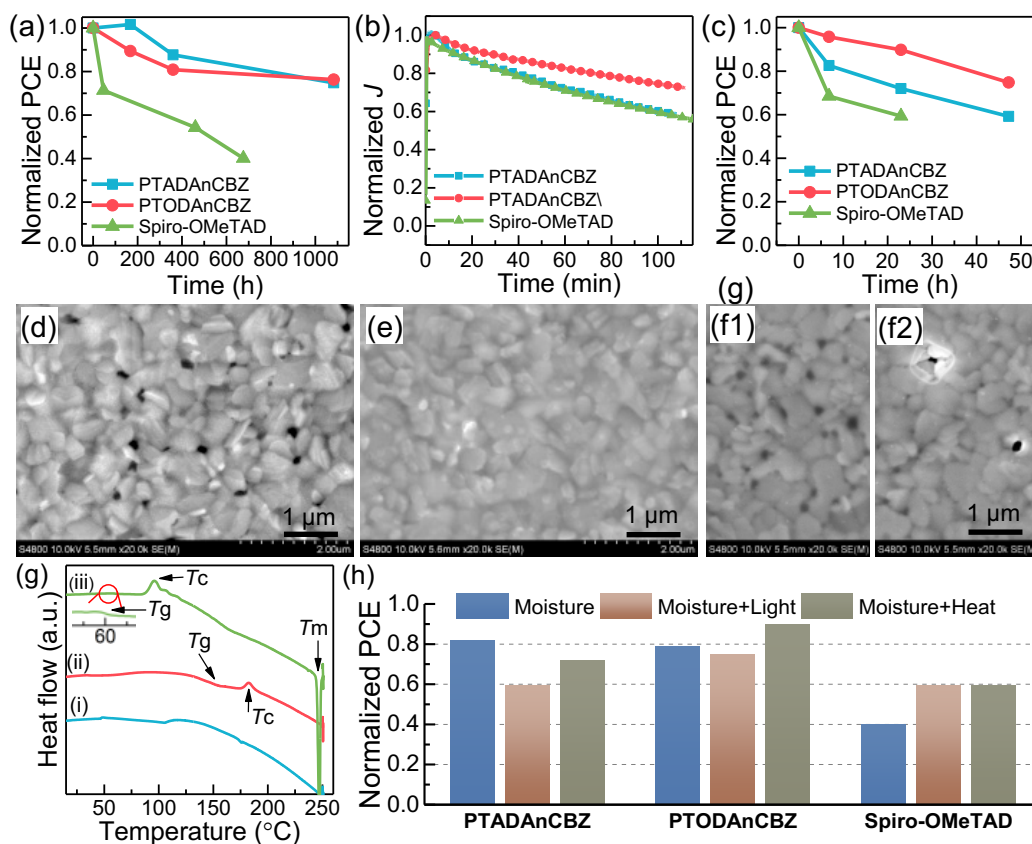

Figure 6. (a) Normalized PCE plots of PSCs with **PTADAnCBZ**, **PTODAnCBZ**, and Spiro-OMeTAD aged under ambient conditions (30 – 70% RH), (b) The maximum power point tracking under moisture and 1-Sun illumination of the unencapsulated device with different HTMs, (c) The normalized PCE plots of PSCs with different HTMs under moisture and continuous heating at 85 °C. Top-view SEM images of perovskite film with (d) **PTADAnCBZ**, (e) **PTODAnCBZ**, and (f1, f2) Spiro-OMeTAD HTMs after aging 100 h at moisture and 85 °C conditions, respectively. (g) The 1st heating DSC curves of doped HTMs: (i) **PTADAnCBZ**, (ii) **PTODAnCBZ**, (iii) Spiro-OMeTAD, (h) Summary of normalized PCE obtained after aging under different conditions.

Second, we tracked the PSC for maximum power point tracking for the unencapsulated devices under moisture (30 – 70% RH) and continuous 1 Sun illumination from white light LED. The device with **PTADAnCBZ**, **PTODAnCBZ**, and Spiro-OMeTAD hold 58.8%, 73.0%, and 58.7% of their initial PCE after 110 min. We noted that **PTODAnCBZ** exhibit improved stability on exposure to moisture and light sustainability as compared to **PTADAnCBZ** and Spiro-OMeTAD.

In a PV device a rise in the temperature during the long-time light-soaking process is inevitable, thermal assessment is pivotal to designed novel HTMs. The PSCs with different HTMs was aged under 85 °C in the glovebox with argon for 10 h. PSCs with **PTADAnCBZ** and **PTODAnCBZ** retained 96.1% and 90.6% of initial PCE, respectively (Figure S14), higher than that of Spiro-OMeTAD (85.3%). Furthermore, we exposed these PSCs to combined stress condition, moisture (30 – 70% RH) and continuous temperature 85 °C. The PCE held 74.8% and 59.2% of the initial value in the case of a PSCs with **PTADAnCBZ** and **PTODAnCBZ** after aging of 47 h, respectively, but 40% of the initial value after aging 20 h was identified for Spiro-OMeTAD. The R_s values of **PTADAnCBZ-** and **PTODAnCBZ-** based PSCs display trivial increase to 1.6 and 1.1 times after aging of nearly 50 h, while for the control device it increases sharply to 1.6 times in just 22 h of ageing (Figure S15). The surface microstructure images of perovskite films with different HTM after aging 100 h are shown (Figure 6e-6g). The perovskite/**PTADAnCBZ** film showed pin-holes and voids, and the perovskite/**PTODAnCBZ** preserved the uniform and homogenous nature, while the perovskite/Spiro-OMeTAD illustrate dense but with small pinholes, or some holes with micrometer size (Figure 5f2), which stems from the accelerating interaction between aggregated lithium salt and moisture under thermal pressure.

It can rapidly depreciate the transport ability and degrade the perovskite layers. t-BP is the only liquid material in the doped HTM layers that will evaporate readily, and the deliquescent and hydrophilic LiTFSI tends to aggregate and absorb moisture and create many voids in the PTADAnCBZ and Spiro-OMeTAD film.[39−42] In contrast, PTODAnCBZ that has the sulfone group with LiTFSI may retard the aggregate process. The reliability of perovskite with **PTADAnCBZ** and **PTODAnCBZ** under different stress conditions (Figure 6h), suggest that **PTODAnCBZ** posseses improved stability as compared to **PTADAnCBZ** and Spiro-OMeTAD.

We also probed the thermal behaviour for HTMs with dopant (lithium salt and *t*-BP) under simulated processing conditions was also investigated. The HTMs and dopants were dissolved in chlorobenzene, dropped into the DSC pans, and placed in the glovebox to evaporate the solvents. Reports suggests that small-molecule based HTMs showed different thermal properties for melted and solution-processed samples.[43] To simulate the thermal behaviour of doped HTM films after deposition on top of perovskite, the first-heating running curves were analysed. Figure 6g, **PTADAnCBZ** (*curve i*) suggests it retains amorphous properties without obvious T_g, which is consistent with the DSC of pristine **PTADAnCBZ** powder. The insignificant decrease from 166 °C to ~ 150 °C was detected for **PTODAnCBZ** (*curve ii*) after introducing dopants, and the crystallization peak (T_c) at 185 °C appears. However, the doped Spiro-OMeTAD (*curve iii*) showed a significant drop in T_g from ~ 120 to 62 °C, an obvious T_c peak at ~ 100°C, and melting of the crystals (T_m) at 240 °C, most possible induced by the liquid-type *t*-BP as a plasticizer.[44]

It is known that the deformation of HTMs arises from crystallization treated at a temperature above T_g. The doped Spiro-OMeTAD display a low T_g (62 °C) and T_c (~ 100°C), leading to the Spiro-OMeTAD-based PSCs the degradation under thermal stress at 85 °C. However, the doped **PTADAnCBZ** films preserve the amorphous properties even under a wide range of temperature,

and doped **PTODAnCBZ** samples have a T_g and T_c, distinctly higher than the thermal stress. The excellent thermal properties of phenothiazine based HTMs will induced improved stability in PSCs.

Phenothiazine-based HTMs displayed on par performance but with improved stability as compared to the Spiro-OMeTAD, validating them as potential alternative HTMs for device fabrication. The cost-effectiveness and notable electrochemical and physicochemical properties will prevail to lower the cost of perovskite-based modules. We estimated the synthesis and purification cost of **PTADAnCBZ** and **PTODAnCBZ** at the laboratory stage (Table S3 – S13), the calculated costs of **PTADAnCBZ** and **PTODAnCBZ** are about ∼ 33.2 € and ∼ 32.1 € per gram, respectively, which is significantly lower than that of Spiro-OMeTAD (about 400 € per gram). Furthermore, the cost per millilitre for **PTODAnCBZ** (**PTODAnCBZ**) is 1.8 € per mL, which is remarkably lower than that of Spiro-OMeTAD (28.9 € per mL). We established the use of cost effective **PTODAnCBZ**, which can expedite the development for PSCs for prototyping.

3. Conclusions

To conclude, innovative small molecules based on the phenothiazine with *N*-position substituting anisole (PTA) or the phenothiazine with *N*-, S- position substituting with position anisole and dioxide (PTO), respectively, as cores, and bis(N^3,N^3,N^6,N^6-tetrakis(4-methoxyphenyl)-9H-carbazole-3,6- diamine (DAnCBZ) group as the arms, were developed as hole selective layers. The **PTODAnCBZ**-based *n-i-p* type perovskite solar cells achieved a higher efficiency than that of **PTADAnCBZ**, which was on par with Spiro-OMeTAD. More importantly, the **PTOADAnCBZ**-based devices showed excellent stability under multi-stress conditions (moisture, continuous light, and heat). The **PTODAnCBZ** consisting of an electron-withdrawing sulfone group is endowed with excellent optoelectrical, thermal, and electrochemical properties as

compared to **PTADAnCBZ** with an electron-donating sulfur atom. Our investigation highlights the advantages of PTO as cost-effective hole selective layers and validates their application for optoelectrical applications.

Conflicts of interest

The authors declare no conflict of interest.

Supporting Information

Detailed device fabrication and characterization, General experimental methods and ^{1}H and ^{13}C NMR and HRMS spectra of all the new compounds, cost calculations, computational results.

References

(1)   NREL Best Research-Cell Efficiencies. *https://www.nrel.gov/ pv/cell-efficiency.html*

(accessed in March, 2021).

(2)   Yoo, J. J.; Seo, G.; Chua, M. R.; Park, T. G.; Lu, Y.; Rotermund, F.; Kim, Y. K.; Moon,

C. S.; Jeon, N. J.; Correa-Baena, J. P.; Bulović, V.; Shin, S. S.; Bawendi, M. G.; Seo, J.

Efficient Perovskite Solar Cells via Improved Carrier Management. *Nature* **2021**, *590*

(7847), 587–593. https://doi.org/10.1038/s41586-021-03285-w.

(3)   Huang, P.; Liu, Y.; Zhang, K.; Yuan, L.; Li, D.; Hou, G.; Dong, B.; Zhou, Y.; Song, B.;

Li, Y. Catechol Derivatives as Dopants in PEDOT:PSS to Improve the Performance of p-

i-n Perovskite Solar Cells. *J. Mater. Chem. A* **2017**, *5* (46), 24275–24281.

https://doi.org/10.1039/c7ta08827b.

(4)   Huang, P.; Yuan, L.; Zhang, K.; Chen, Q.; Zhou, Y.; Song, B.; Li, Y. Room-Temperature

and Aqueous Solution-Processed Two-Dimensional TiS 2 as an Electron Transport Layer

for Highly Efficient and Stable Planar n–i–p Perovskite Solar Cells. *ACS Appl. Mater.*

Interfaces **2018**, *10* (17), 14796–14802. https://doi.org/10.1021/acsami.8b03225.

(5)   Ye, S.; Rao, H.; Zhao, Z.; Zhang, L.; Bao, H.; Sun, W.; Li, Y.; Gu, F.; Wang, J.; Liu, Z.;

Bian, Z.; Huang, C. A Breakthrough Efficiency of 19.9% Obtained in Inverted Perovskite

Solar Cells by Using an Efficient Trap State Passivator Cu(Thiourea)I. *J. Am. Chem. Soc.*

2017, *139* (22), 7504–7512. https://doi.org/10.1021/jacs.7b01439.

(6)   Huang, P.; Chen, Q.; Zhang, K.; Yuan, L.; Zhou, Y.; Song, B.; Li, Y. 21.7% Efficiency

Achieved in Planar n–i–p Perovskite Solar Cells via Interface Engineering with Water-

Soluble 2D TiS 2. *J. Mater. Chem. A* **2019**, *7* (11), 6213–6219.

https://doi.org/10.1039/C8TA11841H.

(7)   Jung, E.H.; Joong Jeon, N.; Young Park, E.; Su Moon, C.; Joo Shin, T.; Yang, T.-Y.;

Hong Noh, J.; Seo, J.; H FTO d-TiO, W. B. Efficient, Stable and Scalable Perovskite

Solar Cells Using Poly(3-Hexylthiophene). *Nature*. 2019. https://doi.org/10.1038/s41586-019-1036-3.

(8) Caliò, L.; Salado, M.; Kazim, S.; Ahmad, S. A Generic Route of Hydrophobic Doping in Hole Transporting Material to Increase Longevity of Perovskite Solar Cells. *Joule* **2018**, *2* (9), 1800–1815. https://doi.org/10.1016/j.joule.2018.06.012.

(9) Gangala, S.; Misra, R. Spiro-Linked Organic Small Molecules as Hole-Transport Materials for Perovskite Solar Cells. *J. Mater. Chem. A* **2018**, *6* (39), 18750–18765. https://doi.org/10.1039/c8ta08503j.

(10) Zhang, J.; Xu, L. J.; Huang, P.; Zhou, Y.; Zhu, Y. Y.; Yuan, N. Y.; Ding, J. N.; Zhang, Z. G.; Li, Y. F. A Simple and Dopant-Free Hole-Transporting Material Based on (2-Ethylhexyl)-9H-Carbazole for Efficient Planar Perovskite Solar Cells. *J. Mater. Chem. C* **2017**, *5* (48), 12752–12757. https://doi.org/10.1039/C7TC03683C.

(11) Xu, L.; Huang, P.; Zhang, J.; Jia, X.; Ma, Z.; Sun, Y.; Zhou, Y.; Yuan, N.; Ding, J. N , N - Di- Para -Methylthiophenylamine-Substituted (2-Ethylhexyl)-9 H -Carbazole: A Simple, Dopant-Free Hole-Transporting Material for Planar Perovskite Solar Cells. *J. Phys. Chem. C* **2017**, *121* (40), 21821–21826. https://doi.org/10.1021/acs.jpcc.7b04469.

(12) Huang, P.; Hernández, A.; Kazim, S.; Ortiz, J.; Sastre-Santos, Á.; Ahmad, S. Molecularly Engineered Thienyl-Triphenylamine Substituted Zinc Phthalocyanine as Dopant Free Hole Transporting Materials in Perovskite Solar Cells. *Sustain. Energy Fuels* **2020**, *4* (12), 6188–6195. https://doi.org/10.1039/D0SE01215G.

(13) Urieta-Mora, J.; García-Benito, I.; Molina-Ontoria, A.; Martín, N. Hole Transporting Materials for Perovskite Solar Cells: A Chemical Approach. *Chem. Soc. Rev.* **2018**, *47* (23), 8541–8571. https://doi.org/10.1039/C8CS00262B.

(14) Calió, L.; Kazim, S.; Grätzel, M.; Ahmad, S. Hole-Transport Materials for Perovskite Solar Cells. *Angew. Chemie Int. Ed.* **2016**, *55* (47), 14522–14545. https://doi.org/10.1002/anie.201601757.

(15) Thokala, S.; Singh, S. P. Phenothiazine-Based Hole Transport Materials for Perovskite Solar Cells. *ACS Omega* **2020**, *5* (11), 5608–5619. https://doi.org/10.1021/acsomega.0c00065.

(16) Grisorio, R.; Roose, B.; Colella, S.; Listorti, A.; Suranna, G. P.; Abate, A. Molecular Tailoring of Phenothiazine-Based Hole-Transporting Materials for High-Performing Perovskite Solar Cells. *ACS Energy Lett.* **2017**, *2* (5), 1029–1034. https://doi.org/10.1021/acsenergylett.7b00054.

(17) Wu, W.; Yang, J.; Hua, J.; Tang, J.; Zhang, L.; Long, Y.; Tian, H. Efficient and Stable Dye-Sensitized Solar Cells Based on Phenothiazine Sensitizers with Thiophene Units. *J. Mater. Chem.* **2010**, *20* (9), 1772–1779. https://doi.org/10.1039/b918282a.

(18) Maciejczyk, M.; Ivaturi, A.; Robertson, N. SFX as a Low-Cost "Spiro" Hole-Transport Material for Efficient Perovskite Solar Cells. *J. Mater. Chem. A* **2016**, *4* (13), 4855–4863. https://doi.org/10.1039/c6ta00110f.

(19) Ding, X.; Chen, C.; Sun, L.; Li, H.; Chen, H.; Su, J.; Li, H.; Li, H.; Xu, L.; Cheng, M. Highly Efficient Phenothiazine 5,5-Dioxide-Based Hole Transport Materials for Planar Perovskite Solar Cells with a PCE Exceeding 20%. *J. Mater. Chem. A* **2019**, *7* (16), 9510–9516. https://doi.org/10.1039/C9TA00654K.

(20) Grigalevicius, S.; Blazys, G.; Ostrauskaite, J.; Grazulevicius, J. V.; Gaidelis, V.; Jankauskas, V. Photoconductive Molecular Glasses Consisting of Twin Molecules. *J. Photochem. Photobiol. A Chem.* **2003**, *154* (2–3), 161–167.

https://doi.org/10.1016/S1010-6030(02)00326-X.

(21)   Huang, P.; Manju; Kazim, S.; Sivakumar, G.; Salado, M.; Misra, R.; Ahmad, S. Pyridine

Bridging Diphenylamine-Carbazole with Linking Topology as Rational Hole Transporter

for Perovskite Solar Cells Fabrication. *ACS Appl. Mater. Interfaces* **2020**, *12* (20), 22881–

22890. https://doi.org/10.1021/acsami.0c03584.

(22)   Lee, D. Y.; Sivakumar, G.; Manju; Misra, R.; Seok, S. Il. Carbazole-Based

Spiro[Fluorene-9,9′-Xanthene] as an Efficient Hole-Transporting Material for Perovskite

Solar Cells. *ACS Appl. Mater. Interfaces* **2020**, *12* (25), 28246–28252.

https://doi.org/10.1021/acsami.0c06318.

(23)   Magomedov, A.; Paek, S.; Gratia, P.; Kasparavicius, E.; Daskeviciene, M.; Kamarauskas,

E.; Gruodis, A.; Jankauskas, V.; Kantminiene, K.; Cho, K. T.; Rakstys, K.; Malinauskas,

T.; Getautis, V.; Nazeeruddin, M. K. Diphenylamine-Substituted Carbazole-Based Hole

Transporting Materials for Perovskite Solar Cells: Influence of Isomeric Derivatives. *Adv.*

Funct. Mater. **2018**, *28* (9), 1–13. https://doi.org/10.1002/adfm.201704351.

(24)   Shi, Y.; Hou, K.; Wang, Y.; Wang, K.; Ren, H. C.; Pang, M. Y.; Chen, F.; Zhang, S. Two

Methoxyaniline-Substituted Dibenzofuran Derivatives as Hole-Transport Materials for

Perovskite Solar Cells. *J. Mater. Chem. A* **2016**. https://doi.org/10.1039/c6ta00976j.

(25)   Li, D.; Shao, J.-Y.; Li, Y.; Li, Y.; Deng, L.-Y.; Zhong, Y.-W.; Meng, Q. New Hole

Transporting Materials for Planar Perovskite Solar Cells. *Chem. Commun.* **2018**, *54* (13),

1651–1654. https://doi.org/10.1039/C7CC08985F.

(26)   Wang, L.; Sheibani, E.; Guo, Y.; Zhang, W.; Li, Y.; Liu, P.; Xu, B.; Kloo, L.; Sun, L.

Impact of Linking Topology on the Properties of Carbazole-Based Hole-Transport

Materials and Their Application in Solid-State Mesoscopic Solar Cells. *Sol. RRL* **2019**,

1900196. https://doi.org/10.1002/solr.201900196.

(27)   Jiang, Q.; Zhang, L.; Wang, H.; Yang, X.; Meng, J.; Liu, H.; Yin, Z.; Wu, J.; Zhang, X.;
        You, J. Enhanced Electron Extraction Using SnO2 for High-Efficiency Planar-Structure
        HC(NH2)2PbI3-Based Perovskite Solar Cells. *Nat. Energy* **2017**, *2* (1), 16177–16183.
        https://doi.org/10.1038/nenergy.2016.177.

(28)   Rakstys, K.; Saliba, M.; Gao, P.; Gratia, P.; Kamarauskas, E.; Paek, S.; Jankauskas, V.;
        Nazeeruddin, M. K. Highly Efficient Perovskite Solar Cells Employing an Easily
        Attainable Bifluorenylidene-Based Hole-Transporting Material. *Angew. Chemie Int. Ed.*
        2016, *55* (26), 7464–7468. https://doi.org/10.1002/anie.201602545.

(29)   Zhao, Y.; Zhang, K.; Wang, Z.; Huang, P.; Zhu, K.; Li, Z.; Li, D.; Yuan, L.; Zhou, Y.;
        Song, B. Comprehensive Study of Sol–Gel versus Hydrolysis–Condensation Methods To
        Prepare ZnO Films: Electron Transport Layers in Perovskite Solar Cells. *ACS Appl.*
        Mater. Interfaces **2017**, *9* (31), 26234–26241. https://doi.org/10.1021/acsami.7b04833.

(30)   Nakar, R.; Ramos, F. J.; Dalinot, C.; Marques, P. S.; Cabanetos, C.; Leriche, P.;
        Sanguinet, L.; Kobeissi, M.; Blanchard, P.; Faure-Vincent, J.; Tran-Van, F.; Berton, N.;
        Rousset, J.; Schmaltz, B. Cyclopentadithiophene and Fluorene Spiro-Core-Based Hole-
        Transporting Materials for Perovskite Solar Cells. *J. Phys. Chem. C* **2019**, *123* (37),
        22767–22774. https://doi.org/10.1021/acs.jpcc.9b05931.

(31)   Bi, D.; Xu, B.; Gao, P.; Sun, L.; Grätzel, M.; Hagfeldt, A. Facile Synthesized Organic
        Hole Transporting Material for Perovskite Solar Cell with Efficiency of 19.8%. *Nano*
        Energy **2016**, *23*, 138–144. https://doi.org/10.1016/j.nanoen.2016.03.020.

(32)   López-Rupérez, F.; Conesa, J. C.; Soria, J. EPR Study of the Alimemazine Cation
        Radical. *Org. Magn. Reson.* **1982**, *20* (3), 162–165.

https://doi.org/10.1002/mrc.1270200310.

(33) Kim, H.-S.; Park, N.-G. Parameters Affecting I – V Hysteresis of CH3NH3PbI3

Perovskite Solar Cells: Effects of Perovskite Crystal Size and Mesoporous TiO2 Layer. *J.

Phys. Chem. Lett.* **2014**, *5* (17), 2927–2934. https://doi.org/10.1021/jz501392m.

(34) Rakstys, K.; Abate, A.; Dar, M. I.; Gao, P.; Jankauskas, V.; Jacopin, G.; Kamarauskas, E.;

Kazim, S.; Ahmad, S.; Grätzel, M.; Nazeeruddin, M. K. Triazatruxene-Based Hole

Transporting Materials for Highly Efficient Perovskite Solar Cells. *J. Am. Chem. Soc.*

2015, *137* (51), 16172–16178. https://doi.org/10.1021/jacs.5b11076.

(35) Li, J.; Jiu, T.; Duan, C.; Wang, Y.; Zhang, H.; Jian, H.; Zhao, Y.; Wang, N.; Huang, C.;

Li, Y. Improved Electron Transport in MAPbI3 Perovskite Solar Cells Based on Dual

Doping Graphdiyne. *Nano Energy* **2018**, *46*, 331–337.

https://doi.org/10.1016/j.nanoen.2018.02.014.

(36) Kyaw, A. K. K.; Wang, D. H.; Gupta, V.; Leong, W. L.; Ke, L.; Bazan, G. C.; Heeger, A.

J. Intensity Dependence of Current–Voltage Characteristics and Recombination in High-

Efficiency Solution-Processed Small-Molecule Solar Cells. *ACS Nano* **2013**, *7* (5), 4569–

4577. https://doi.org/10.1021/nn401267s.

(37) Shi, J.; Dong, J.; Lv, S.; Xu, Y.; Zhu, L.; Xiao, J.; Xu, X.; Wu, H.; Li, D.; Luo, Y.; Meng,

Q. Hole-Conductor-Free Perovskite Organic Lead Iodide Heterojunction Thin-Film Solar

Cells: High Efficiency and Junction Property. *Appl. Phys. Lett.* **2014**, *104* (6), 063901.

https://doi.org/10.1063/1.4864638.

(38) Zhang, H.; Wang, H.; Chen, W.; Jen, A. K. Y. CuGaO2: A Promising Inorganic Hole-

Transporting Material for Highly Efficient and Stable Perovskite Solar Cells. *Adv. Mater.*

2017, *29* (8), 1–8. https://doi.org/10.1002/adma.201604984.

(39) Ren, G.; Han, W.; Deng, Y.; Wu, W.; Li, Z.; Guo, J.; Bao, H.; Liu, C.; Guo, W. Strategies of Modifying Spiro-OMeTAD Materials for Perovskite Solar Cells: A Review. *J. Mater. Chem. A* **2021**, *9*, 4589−4625.

(40) Hawash, Z.; Ono, L. K.; Raga, S. R.; Lee, M. V.; Qi, Y. Air- Exposure Induced Dopant Redistribution and Energy Level Shifts in Spin-Coated Spiro-Meotad Films. *Chem. Mater.* **2015**, *27*, 562−569.

(41) Pham, N. D.; Shang, J.; Yang, Y.; Hoang, M. T.; Tiong, V. T.; Wang, X.; Fan, L.; Chen, P.; Kou, L.; Wang, L.; Wang, H. Alkaline- Earth Bis(Trifluoromethanesulfonimide) Additives for Efficient and Stable Perovskite Solar Cells. *Nano Energy* **2020**, *69*, 104412.

(42) Juarez-Perez, E. J.; Leyden, M. R.; Wang, S.; Ono, L. K.; Hawash, Z.; Qi, Y. Role of the Dopants on the Morphological and Transport Properties of Spiro-MeOTAD Hole Transport Layer. *Chem. Mater.* **2016**, *28*, 5702−5709.

(43) Malinauskas, T.; Tomkute-Luksiene, D.; Sens, R.; Daskeviciene, M.; Send, R.; Wonneberger, H.; Jankauskas, V.; Bruder, I.; Getautis, V. Enhancing Thermal Stability and Lifetime of Solid-State Dye-Sensitized Solar Cells via Molecular Engineering of the Hole-Transporting Material Spiro-OMeTAD. *ACS Appl. Mater. Interfaces* **2015**, *7* (21), 11107−11116. https://doi.org/10.1021/am5090385.

(44) Jeon, N. J.; Na, H.; Jung, E. H.; Yang, T. Y.; Lee, Y. G.; Kim, G.; Shin, H. W.; Il Seok, S.; Lee, J.; Seo, J. A Fluorene-Terminated Hole-Transporting Material for Highly Efficient and Stable Perovskite Solar Cells. *Nat. Energy* **2018**, *3* (8), 682–689. https://doi.org/10.1038/s41560-018-0200-6.